



The relationship between atmospheric boundary layer and temperature inversion layer and their aerosol capture capabilities



Boming Liu^a, Xin Ma^{a,*}, Yingying Ma^a, Hui Li^a, Shikuan Jin^a, Ruonan Fan^a, Wei Gong^b

^a State Key Laboratory of Information Engineering in Surveying, Mapping and Remote Sensing (LIESMARS), Wuhan University, Wuhan 430079, China

^b School of Electronic Information, Wuhan University, Wuhan 430079, China

ARTICLE INFO

Keywords:

AOD
Lidar
Boundary layer
Temperature inversion layer

ABSTRACT

The vertical distribution of aerosols is an important factor in the study of urban environment pollution. However, whether the aerosol is captured by the atmospheric boundary layer or the temperature inversion layer remains unclear. In this study, the relationship between atmospheric boundary layer and temperature inversion layer was investigated based on the micropulse lidar and radiosonde measurements from February 2017 to September 2021 at atmospheric radiation measurement southern great plains site. The results revealed that for each residual layer height (RLH), stable boundary layer height (SBLH) and mixing layer height (MLH), the occurrence frequency of inversion layer within its 0.3 km range is 58, 58 and 68%, respectively. Moreover, the relative error of the MLH, RLH and SBLH relative to the inversion layer height (ILH) under different inversion strength (ΔT) conditions were investigated. The mean relative errors for MLH-ILH, RLH-ILH and SBLH-ILH are -4.13 ± 9.69 , -2.26 ± 9.36 and $-1.81 \pm 15.87\%$, respectively. The result indicates that the ILH is generally higher than the top of the aerosol layer, and this phenomenon becomes more obvious as the ΔT increased. Finally, the aerosol capture capabilities of different layers are compared. The determination coefficient (R^2) between AOD below RLH (MLH) and AOD below ILH are 0.47 (0.58). When the ΔT is larger than 2 °C, the R^2 between AOD below RLH (MLH) and AOD below ILH has been obviously improved, increasing to 0.81 (0.90). By contrast, when the ΔT is smaller than 2 °C, the aerosol capture ability of RLH (MLH) is larger (smaller) than that of ILH. It indicates that the temperature inversion intensity is a key factor in determining the aerosol capture ability. These findings have implications for improving our understanding of the vertical distribution of aerosols and its controlling factors.

1. Introduction

Aerosols play an important role in human activities and the natural environment (Ramanathan et al., 2001; Bourgeois et al., 2018). Natural and anthropogenic aerosols can affect global climate change by scattering and absorbing solar radiation and changing the radiation characteristics of clouds (Koren et al., 2014; Che et al., 2014; Shi et al., 2021; Yang et al., 2021). Aerosol pollution caused by industrial emissions and sandstorms can also cause environmental problems and adversely affect human health (Wang et al., 2021; Yin et al., 2020; Liu et al., 2019). Moreover, the uneven distribution of aerosols in the vertical direction brings the challenges and uncertainties to ecological environment protection and weather forecasting (Guo et al., 2019; Liu et al., 2017; Ma et al., 2021a). Therefore, it is very important to study the vertical distribution of aerosols.

Numerous research has been carried out to investigate the vertical distribution of aerosols (Guo et al., 2016; Fan et al., 2019; Liu et al., 2020; Ma et al., 2021b; Zhu et al., 2021). Liu et al. (2017) studied the vertical distribution of aerosols over Wuhan based on lidar measurement, and pointed out that most aerosols are concentrated within 0–3 km near the surface. Bourgeois et al. (2018) investigated the aerosol optical depth (AOD) in the boundary layer and free troposphere within the globe. They indicated that the AOD in the boundary layer account for 69% of the total AOD. Moreover, Liu et al. (2020) and Shi et al. (2020) also indicated that a large fraction of aerosols remain in the residual layer during the nighttime, which may even act as a source for boundary layer aerosol formation the following day. These studies have given us a preliminary understanding of the vertical distribution of aerosols.

With further research, some studies have begun to investigate the

* Corresponding author.

E-mail address: maxinwhu@whu.edu.cn (X. Ma).

driving factors of surface aerosol accumulation and diffusion, such as the role of atmospheric boundary layer and temperature inversions on the surface aerosol (Sun et al., 2012, 2013; Liu et al., 2019; Guo et al., 2020; Zhao et al., 2021; Ma et al., 2022). Tang et al. (2016) and Liu et al. (2021) studied the effect of atmospheric boundary layer on air pollution in Beijing based on the ceilometer observation. They pointed out that the boundary layer height affects the vertical diffusion capability that determines the surface pollutants concentration. Ding et al. (2016) discovered the dome effect of the atmosphere boundary layer. Aerosols (especially black carbon) can affect the development of the atmospheric boundary layer through its radiation effect, leading to two-way feedback between air pollution and the atmospheric boundary layer (Ma et al., 2020). Moreover, some studies have investigated the effect of inversions on the surface aerosols (Wallace and Kanaroglou, 2009; Wang et al., 2018). Prasad et al. (2022) compared the influence of boundary layer and inversion layer on the vertical extent of aerosols, and indicated that the strongest temperature inversion is the deciding factor for the aerosol vertical distribution rather than the boundary layer height. In addition, Sun et al. (2012) and Zhang et al. (2011) conducted field studies at various locations over China, also revealed that aerosols are accumulated mainly at the bottom of the inversion layer. From all these studies, the impact of boundary layer and temperature inversions on the surface aerosol loading is well understood but the aerosol capture capabilities of the boundary layer and the inversion layer remains unexplored.

In this study, long-term micropulse lidar and radiosonde measurements from February 2017 to September 2021 at atmospheric radiation measurement southern great plains (ARM SGP) site, are used to investigate the relationship between atmospheric boundary layer and temperature inversion layer. The main objective of this work was to compare the aerosol capture capabilities of the boundary layer and the inversion layer. The results can help us understand the vertical distribution of aerosols and its controlling factors. This paper proceeds as follows: Section 2 describes the MPL and RS observation data. Section 3 describes the calculation method in terms of boundary layer heights, IL and AOD. Results and discussion are presented in Section 4, and a brief conclusion is given in Section 5.

2. Instruments and data

2.1. Micropulse lidar data

The aerosol backscatter profiles are provided by the MPL system at ARM SGP site ($36^{\circ}36' N, 97^{\circ}29' W$). The wavelength of the MPL system is 532 nm, and it is equipped with both parallel and perpendicular polarization receiving channels. The vertical and temporal resolution of raw data are 15 m and 10 s, respectively. Given the effect of the overlap, there is a 150 m near-surface blind zone. Detailed parameters of the MPL system can be seen in previous study (Campbell et al., 2002, 2003). The MPL data are collected from February 2017 to September 2021. Following the standard processes, the normalized signal (NS) can be obtained from the raw MPL data by background subtraction, saturation, overlap, after-pulse, and range corrections (Welton et al., 2000, 2001). In here, the NS is averaged in 1-h intervals to reduce the effects of background noise. Moreover, according to the MPL measurements and the quality-control flags, the erroneous data and rainy cases are eliminated from our analysis. To ensure that the atmosphere contains a certain amount of aerosol for further research, the cases with AOD less than 0.1 are also removed. After the screening process, a total of 1998 hourly profiles are obtained.

2.2. Radiosonde data

The temperature profiles are obtained from RS at the SGP site. RS launches took place at least four times per day at 05:30, 11:30, 17:30, and 23:30 coordinated universal time (UTC). The RS can measure the

profile data of atmospheric temperature, humidity, wind speed and pressure (Guo et al., 2020, 2021). The vertical resolution of record data point is approximately 20 m. In this study, the RS data are also collected from February 2017 to September 2021 to match with MPL data. Moreover, the erroneous data and invalid cases are eliminated based on the quality-control flags.

3. Methods

3.1. Retrieval method of different aerosol layer heights

The atmospheric boundary layer is in the mixing layer (ML) state during the daytime, and evolves into the stable boundary layer (SBL) and residual layer (RL) at nighttime (Stull, 1988; Liu et al., 2020). Due to the fact that there is a sharp signal decrease from the PBL upper boundary to the free troposphere, the MPL system can capture the aerosol layer height based on the NS profile (Seibert et al., 2000). In this study, the gradients method is used to calculate the aerosol layer height from the lidar data (Steyn et al., 1999; Liu et al., 2021). For the nighttime (00:00–12:00 UTC), we firstly identify the local minimum value in the NS gradient profile (range: 0.25–3.5 km). Following previous study, a dynamic threshold is applied to exclude the effect of noise (Su et al., 2020). The shot noise is induced by background light and dark currents in each profile (Welton and Campbell, 2002; Whiteman et al., 2006). To avoid noise effects, the local minimum value must be lower than the threshold. As shown in Fig. 1a, the blue circles and red dotted line represent the effective local minimum value and threshold, respectively. Then, the first and last height of these local minimum values are regarded as SBL height (SBLH) and RL height (RLH). If there is only one effective local minimum value detected, it is considered that the RLH and SBLH are the same. By contrast, for the daytime (13:00–23:00 UTC), the height of minimum value in the NS gradient profile is regarded as ML height (MLH), as shown in Fig. 1b.

3.2. Retrieval method of IL

The temperature inversion parameters, such as inversion layer height (ILH), inversion depth and inversion strength, are estimated from the RS measurement. The IL is identified from the gradient change of the temperature profile (Kahl, 1990; Serreze et al., 1992). When there is a value greater than 0 on the temperature gradient profile, it is considered that a temperature inversion has occurred. The height of maximum value in the temperature gradient profile is regarded as ILH. Typical temperature profiles along with their gradients variation observed on 26 July 2019 at 23:30 UTC is shown in Fig. 1c. In this case, the blue circles and blue line represent the maximum value and ILH, respectively. The height at which the temperature start increasing (decreasing) is defined as inversion base (top) height. The temperature difference between the inversion base and top is termed as inversion strength (ΔT) and the height difference is termed as inversion depth (ΔZ). This method is applied to all the RS profiles during 2017 to 2021 to calculate the temperature inversion parameters. In addition, the relationship between ΔT and ΔZ is investigated, as seen in Fig. S1. The exponential increase of the ΔZ as ΔT values increased, with R^2 values of approximately 0.78. This result indicates that the ΔZ and ΔT have a strong positive correlation.

3.3. Retrieval method of AOD

According to the Fernald method and lidar equation, the aerosol extinction coefficient can be obtained to calculate AOD (Fernald, 1984). Kafle and Coulter (2013) pointed out that the lidar ratio at SGP site range from 15 sr to 75 sr with most common values between 28 sr and 35 sr. Therefore, the lidar ratio and calibration height in here are set as 30 sr and 6 km, respectively. Moreover, due to the effect of the overlap factor, the aerosol extinction coefficient profile from 0 to 150 m were

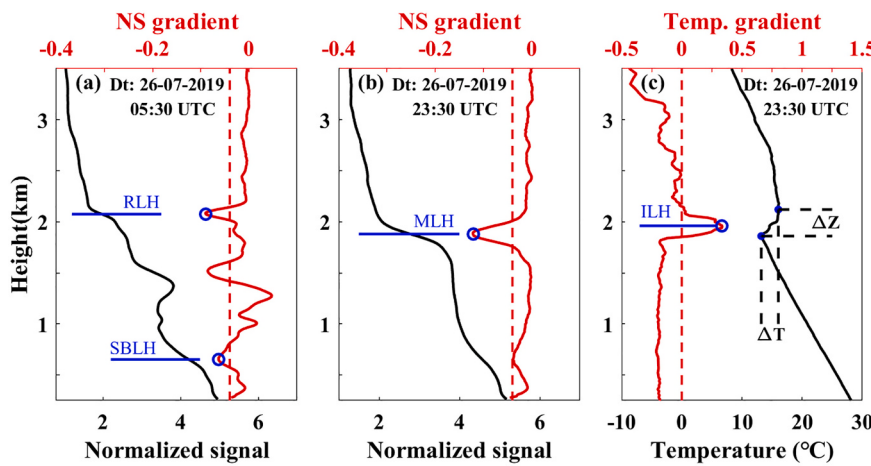


Fig. 1. The vertical profile of normalized signal (black) and NS gradient profile (red) observed on 26 January 2019 at (a) 05:30 UTC and (b) 23:30 UTC over SGP site. (c) The vertical profile of temperature (black) and temperature gradient profile (red) observed on 26 January 2019 at 23:30 UTC over SGP site. Blue and red dotted lines represent the different layer height and threshold value, respectively. (For interpretation of the references to colour in this figure legend, the reader is referred to the web version of this article.)

removed. To correct the overlap function, we extend the aerosol extinction coefficient at 150 m to the surface to reduce the effect of overlap. The aerosol extinction coefficient profile in the 0–6 km was then obtained. Finally, the AOD is the integral of the extinction coefficient along the optical path between r_1 and r_2 (Liu et al., 2017):

$$AOD = \int_{r_1}^{r_2} \alpha(r) dr \quad (1)$$

In this study, we focus on that how much aerosol can be captured by the boundary layer or the temperature inversion. Therefore, the AODs below ML, RL and IL are calculated to compare with each other. The r_1 is set as 0, and r_2 set as MLH, RLH and IL, respectively.

4. Results and discussion

4.1. Case study

Fig. 2 shows a typical case on 24 July 2019. **Fig. 2a** shows the aerosol backscatter profiles and boundary layer height retrievals. The black solid dotted line and the dashed dotted line at nighttime (00:00–12:00 UTC) represent SBLH and RLH, respectively. The black solid dotted line at daytime (13:00–23:00 UTC) represents MLH. The red stars is the ILH retrieved from RS measurement. The aerosols are mainly concentrated in the ML during the daytime. By contrast, during the nighttime, most of aerosols are below the SBL and part of aerosols are concentrated in the RL. This phenomenon is consistent with the diurnal variation of aerosol (Liu et al., 2020; Shi et al., 2020). Combined with RS measurement, **Fig. 2b** and c show the vertical distribution of aerosol backscatter and

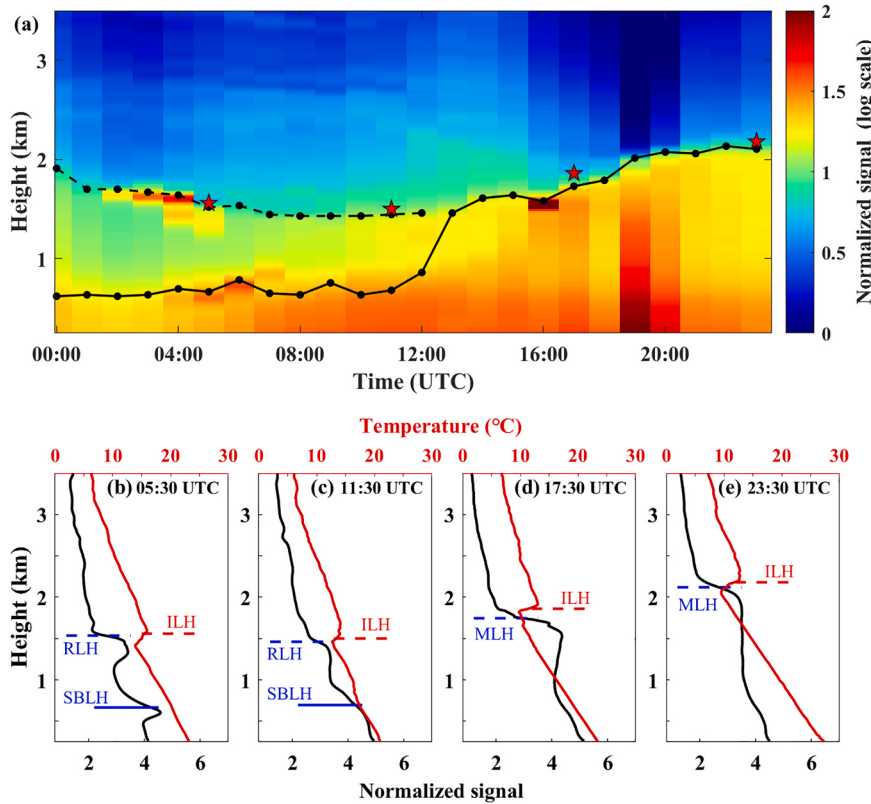


Fig. 2. Case study on 24 July 2019: (a) time–height cross section of normalized signal (log scale). Red star and black dotted line represent the ILH and RLH, respectively. Black line represents the SBLH at nighttime (00:00–12:00 UTC) and MLH at daytime (13:00–23:00 UTC). The vertical profile of normalized signal (black) and temperature profile (red) observed on at (b) 05:30, (c) 11:30, (d) 17:30 and (e) 23:30 UTC over SGP site. (For interpretation of the references to colour in this figure legend, the reader is referred to the web version of this article.)

temperature profiles at nighttime. It can find that the ILH is similar to RLH, but there is no temperature inversion at the SBLH. Similarly, the ILH is consistent with MLH at daytime (Fig. 2d and f). These results indicate that the top of the aerosol layer often accompanied by IL. This is due to the temperature inversion layer can capture moisture and aerosols, so there is often a temperature inversion on the top of the boundary layer (Seibert et al., 2000; Liu et al., 2018).

Fig. 3 shows some cases under the multiple or no IL conditions. The top panels represent vertical distribution of the aerosol backscatter (black line) and temperature (red line) profiles. The bottom panels are the corresponding aerosol backscatter (black line) and temperature (red line) gradient profile. Fig. 3a shows the case study at nighttime on 23 March 2017. The IL appears at both RLH and SBLH. The case study under the multiple IL conditions at daytime can be seen in Fig. 3b. The higher ILH is similar to MLH. Moreover, there is a corresponding effective local minimum value on the aerosol backscatter gradient profile near the lower ILH. It indicates that there is a top of aerosol layer at the lower ILH. Fig. 3c and d show the case studies under no IL conditions. It can see that although there is no IL in temperature profiles, the RLH, SBLH and MLH can still be reversed from the aerosol backscatter gradient profiles. It indicates that the aerosols can form a corresponding boundary layer structure even there is no IL. This creates a basic curiosity to investigate the relationship between atmospheric boundary layer and temperature inversion layer.

4.2. Occurrence frequency of boundary layer and IL and their associations

In this section, we calculated the frequency of occurrence of

boundary layer and IL to investigate the relationship between the boundary layer and the temperature inversion layer. Moreover, for each MLH, RLH or SBLH, we check whether there is a IL within its 0.3 km range. Similarly, for each ILH, we check whether there is an effective local minimum value on the aerosol backscatter gradient profile within its 0.3 km range.

Fig. 4a shows the number of observations of different aerosol layers and the corresponding IL. Black line shows the frequency of occurrence of IL. For all observations (1998 cases), 83% of samples are accompanied by IL. Specific to RL, SBL and ML, the frequency of occurrence of IL is 58%, 58% and 68%, respectively. The number of observations of IL and the corresponding aerosol layer is shown in Fig. 4b. The numbers of observations of IL under 05:30, 11:30, 17:30 and 23:30 UTC are 431, 390, 398 and 439, respectively. The Frequency of occurrence of corresponding aerosol layer is 82%, 85%, 87% and 88%, respectively. These results confirm that the boundary layer structure can be obtained from aerosol backscatter profiles even without the IL structure. In contrast, the appearance of the IL means that there is a high probability that the top of the aerosol layer will appear near the ILH. Moreover, the effect of ΔT and ΔZ on the frequency of occurrence of corresponding aerosol layer are investigated. With the ΔT increased, the frequency of occurrence of corresponding aerosol layer increases from 76% to 91% (Fig. 4c). Due to there is a strong positive correlation between the ΔZ and ΔT (Fig. S1), the effect of ΔZ on the frequency of occurrence of corresponding aerosol layer is similar to that of ΔT . The frequency of occurrence of corresponding aerosol layer increased from 75% to 91% with the ΔZ increased (Fig. 4d). It indicates that the greater the intensity of the IL, the more aerosols can be captured, which is more conducive to the formation of the top of the aerosol layer. Previous studies also point

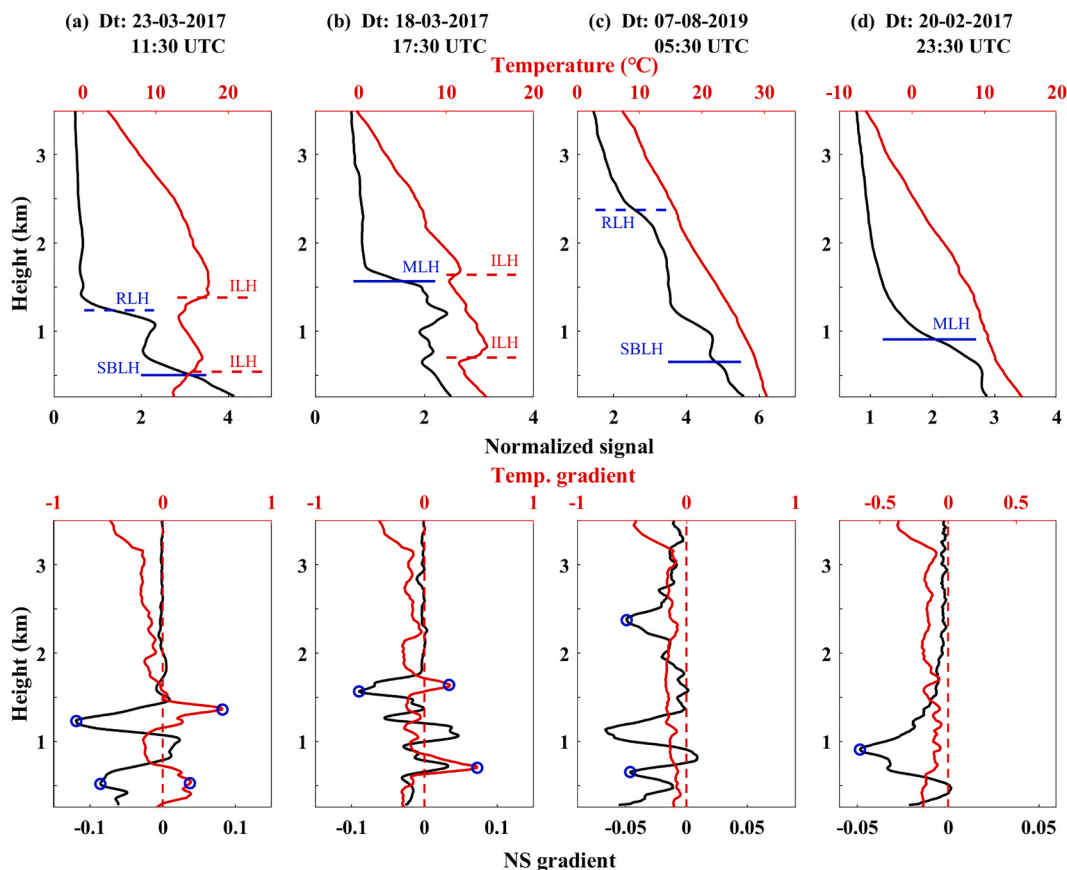


Fig. 3. The vertical profile of normalized signal (black) and temperature profile (red) observed (a) on 23 March 2017 at 11:30 UTC, (b) on 18 March 2017 at 17:30 UTC, (c) on 7 August 2019 at 05:30 UTC, and (d) on 20 February 2017 at 23:30 UTC over SGP site. The corresponding vertical profile of normalized signal gradient (black) and temperature gradient profile (red) are shown in the bottom row. (For interpretation of the references to colour in this figure legend, the reader is referred to the web version of this article.)

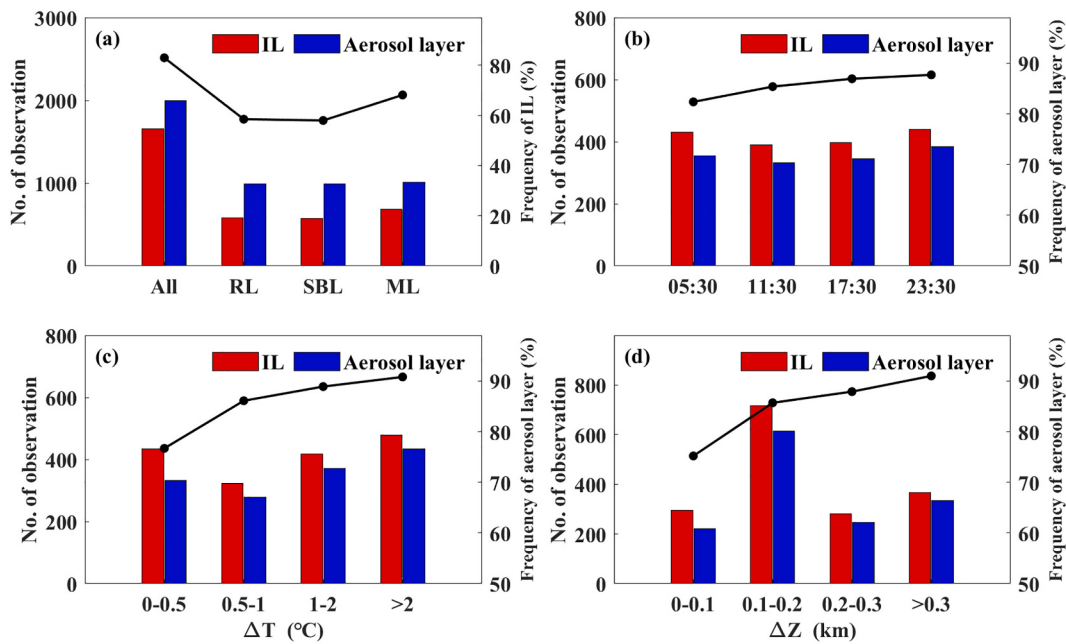


Fig. 4. (a) Total observation number of aerosol profiles (blue bars) and the profiles that occur the temperature inversion (red bars) under different boundary layer conditions. Total observation number of the temperature inversion (red bars) and the corresponding aerosol layer (blue bars) under different (b) time, (c) inversion strengths and (d) inversion depth. Black line represents the frequency of occurrence. (For interpretation of the references to colour in this figure legend, the reader is referred to the web version of this article.)

out that the aerosols are accumulated mainly at the bottom of the inversion layer (Zhang et al., 2011; Sun et al., 2012). The accumulation of aerosol at the bottom of IL can form a gradient change on the aerosol backscatter profile, which will affect the inversion of the boundary layer height (Liu et al., 2018; Li et al., 2021).

Fig. 5 shows the relative error between different boundary layer height and ILH under different ΔT conditions. The gray point and red line show the sample points and mean relative error, respectively. Fig. 5a shows the relative error between MLH and ILH with the ΔT increased. The mean relative error for all samples is -4.13 ± 9.69 . With the ΔT increased, the mean relative errors for each bin are -3.25 ± 10.34 , -5.11 ± 8.91 and -6.09 ± 7.48 , respectively. For RLH and ILH (Fig. 5b), the mean relative error for all samples is -2.26 ± 9.36 . The mean relative errors for each bin are -1.94 ± 9.31 , -2.29 ± 9.75 and -4.51 ± 8.77 , respectively. Fig. 5c shows the relative error between SBLH and ILH with the ΔT increased. The mean relative error for all samples and each bin are -1.81 ± 15.87 , -1.59 ± 15.85 , -1.31 ± 17.65 and -3.86 ± 12.79 , respectively. Two phenomena can be found from these results. One is that the ILH is generally higher than the height of boundary layers. This is due to the aerosols cannot break through the

IL in the vertical direction in most cases, and the IL exists at the top of boundary layer like a cover (Wallace and Kanaroglou, 2009; Prasad et al., 2022). On the other hand, with the ΔT increased, the phenomenon of ILH higher than the height of boundary layers becomes more obvious. This may be related to the method of calculating ILH. The ILH is identified as height of maximum value in the temperature gradient profile, instead of the bottom height of the IL (Section 3.2). This means that the ΔZ becomes larger when ΔT becomes larger. The difference between ILH and the bottom of the IL will become larger, causing that the ILH is higher than the height of the boundary layer.

4.3. Aerosol capture capabilities of different layers

In this section, we compare the AOD below the different layer heights to investigate which layer can capture more aerosols. Previous studies indicate that the aerosols mainly exist in ML during the daytime and in RL at nighttime (Liu et al., 2020; Shi et al., 2020). Therefore, we only calculate the AOD below RLH, MLH and ILH here. In addition, for each temperature profile, if there are multiple IL, only the height of maximum value in the temperature gradient profile is regarded as ILH.

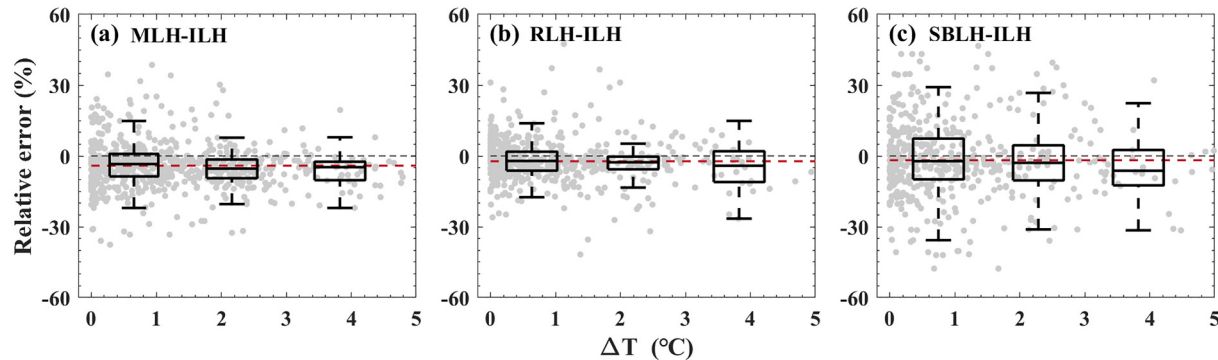


Fig. 5. Relative error of (a) MLH, (b) RLH and (c) SBLH relative to ILH shown as a function of inversion strengths. The gray point and mean relative error, respectively. (For interpretation of the references to colour in this figure legend, the reader is referred to the web version of this article.)

Fig. 6 shows the AOD below the different layer heights under different conditions. The orange, red and blue box represent the AOD below RLH, MLH and ILH, respectively. **Fig. 6a** shows the comparison between the AOD below RLH and corresponding ILH under different season. The mean AODs below RLH (ILH) in spring, summer, autumn and winter are 0.16 (0.13), 0.19 (0.14), 0.16 (0.13) and 0.14 (0.14), respectively. The mean AOD below RLH is similar to that of ILH in winter, and slightly larger in other seasons. By contrast, the mean AODs below MLH (ILH) in four seasons are 0.15 (0.17), 0.18 (0.19), 0.17 (0.18) and 0.16 (0.16), respectively. The mean AOD below MLH is slightly less than that of ILH except winter. Combined with the seasonal variations of temperature inversion intensity (Fig. S2), the average temperature inversion intensity is the largest in winter and the smallest in summer. It indicates that the temperature inversion intensity can affect the content of AOD below different layers. **Fig. 6c** and e show the comparison between the AOD below RLH and corresponding ILH under different ΔT and ΔZ conditions. With the ΔT increased, the mean AODs below RLH (ILH) for each box are 0.17 (0.13), 0.18 (0.13), 0.18 (0.18) and 0.14 (0.13), respectively. Moreover, the mean AODs below RLH (ILH) for each box are 0.18 (0.13), 0.17 (0.13), 0.18 (0.17) and 0.14 (0.13) with the ΔZ increased. It indicates that the difference between AOD below RLH and AOD below ILH is decreased with the temperature inversion intensity increased. This phenomenon also occurs in the MLH and the corresponding ILH (**Fig. 6d** and f). With the temperature inversion intensity increased, the mean AODs below MLH is similar to that of ILH.

Fig. 7 illustrates the correlations between AOD below different layer heights and the AOD below ILH. **Fig. 7a** (**7b**) shows the liner correlation between AOD below RLH (MLH) and AOD below ILH. The gray solid line, gray dotted line, and colour bar represent the linear fitting curve,

1:1 reference line, and ΔT , respectively. The determination coefficient and sample numbers between AOD below RLH (MLH) and AOD below ILH are 0.47 (0.58) and 811 (829), respectively. It can find that the sample with larger ΔT is more close to the reference line. Moreover, the AOD below RLH (MLH) is larger (smaller) than the AOD below ILH when the ΔT is small. **Fig. 7c** (**7d**) shows the liner correlation between AOD below RLH (MLH) and AOD below ILH when the ΔT is larger than 2 °C. The determination coefficient between AOD below RLH (MLH) and AOD below ILH has been obviously improved, increasing to 0.81 (0.90). This phenomenon also happened when we changed ΔT to ΔZ (Fig. S3). The determination coefficient between AOD below RLH (MLH) and AOD below ILH is also improved when the ΔT is larger than 0.2 km. These results confirm that the temperature inversion intensity is the key factor in determining whose aerosol capture ability is stronger. [Prasad et al. \(2022\)](#) also indicates that the strongest temperature inversion is the deciding factor for the aerosol vertical distribution.

To further quantify the impact of temperature inversion intensity, the determination coefficients between AOD below different layer heights and AOD below ILH are calculated when the ΔT or ΔZ is larger than a certain threshold (**Fig. 8**). The determination coefficient gradually increases with the increase of ΔT or ΔZ , and finally remains at a high value around 0.8. The result indicates that the aerosol capture ability of RLH or MLH is similar to that of ILH when the temperature inversion intensity is large. This is due to the aerosol is captured below the IL, which leads to a large gradient in the aerosol backscatter signal at the bottom of the IL ([Seibert et al., 2000; Su et al., 2020](#)). When this gradient is large enough, the height which this gradient occurred is recognized as MLH during the daytime, and is regarded as SBLH or RLH at nighttime. Moreover, the SBLH may be same as RLH when strong temperature inversion occurs. Therefore, the AOD below RLH or MLH is consistent

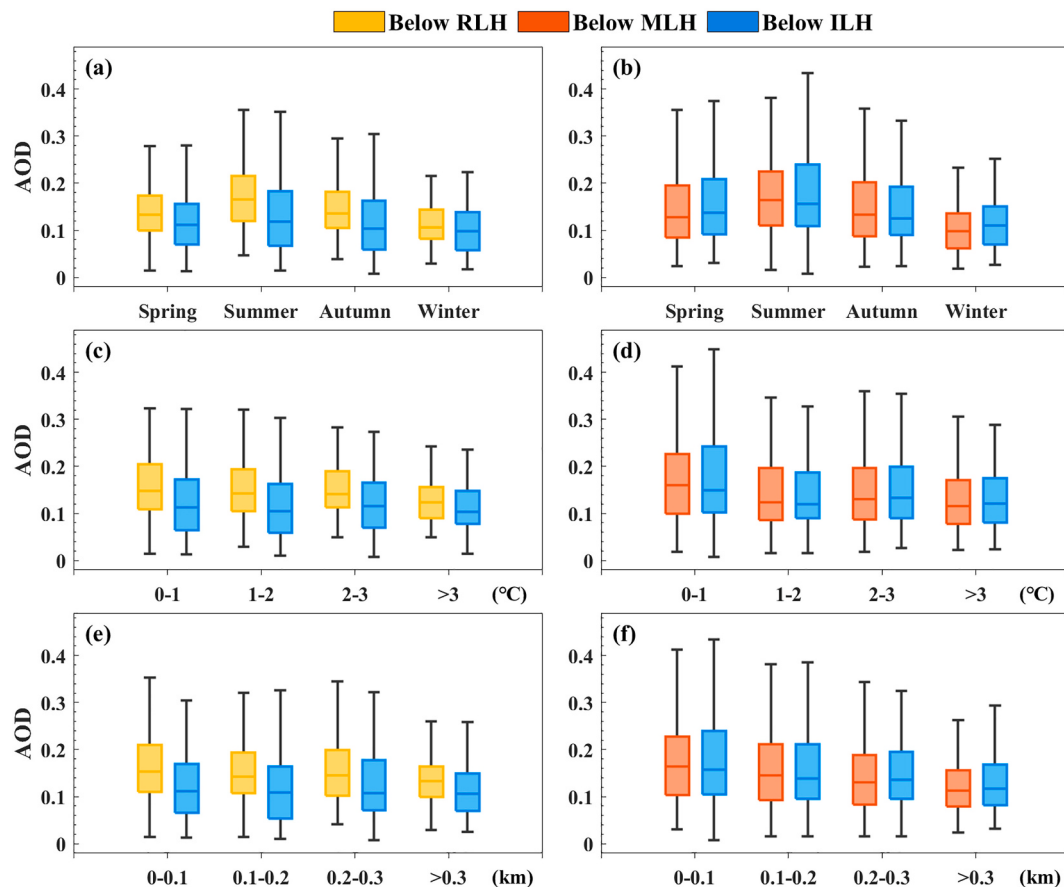


Fig. 6. Comparison of the AOD below RLH and AOD below ILH at different (a) season, (c) inversion strengths and (e) inversion depth. (b), (d) and (f) same as (a), (c) and (e) but for the comparison of the AOD below MLH and AOD below ILH.

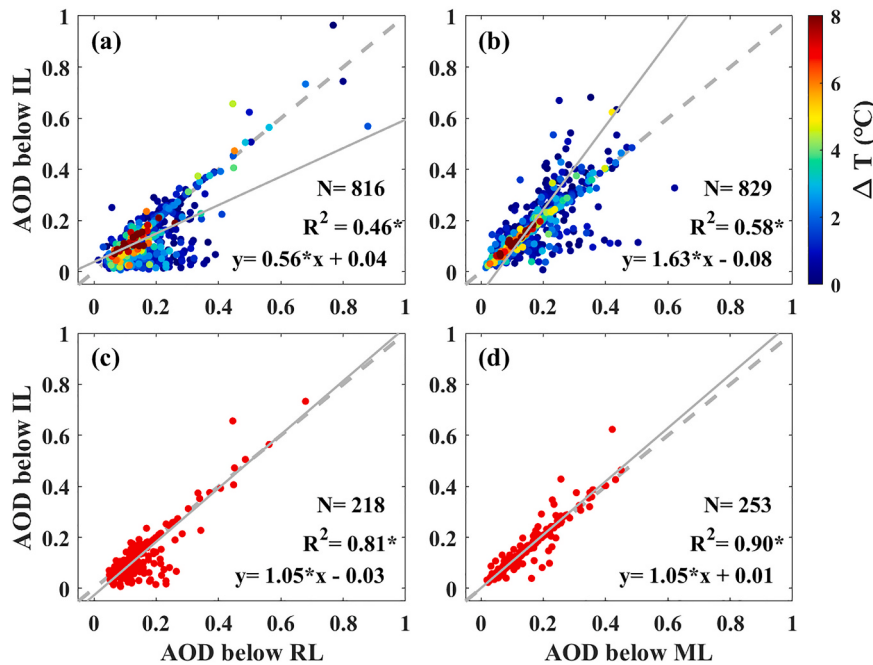


Fig. 7. Relationship between (a)AOD below RL and AOD below IL and (b) AOD below ML and AOD below IL with changes in inversion strengths. Relationship between (c)AOD below RL and AOD below IL and (d) AOD below ML and AOD below IL when the inversion strengths is larger than 2 °C. The asterisks indicate that it passed the significance test ($P < 0.05$).

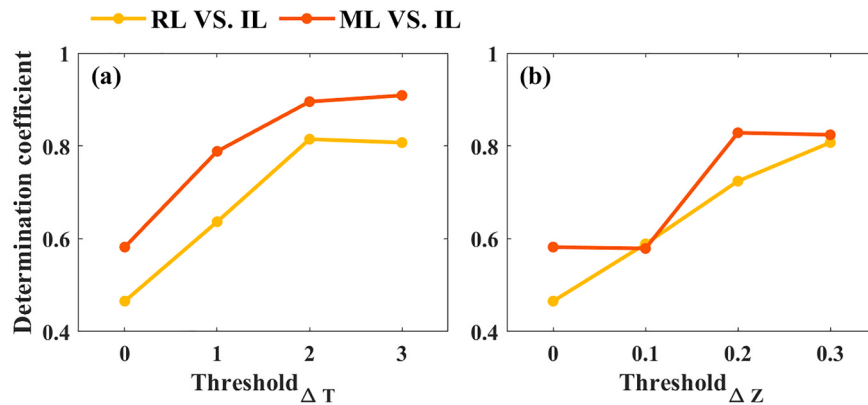


Fig. 8. Determination coefficients between AOD below different boundary layer and AOD below IL under different (a) $\text{threshold}_{\Delta T}$ and (b) $\text{threshold}_{\Delta Z}$. The orange and red line show the AOD below RL and AOD below IL, respectively. (For interpretation of the references to colour in this figure legend, the reader is referred to the web version of this article.)

with that of ILH when the intensity of IL is large. This also explains why some studies have observed that pollutants are concentrated under the IL (Zhang et al., 2011; Wang et al., 2018), and some studies have pointed out that the pollutants are concentrated under the boundary layer (Tang et al., 2016; Liu et al., 2018). When the aerosol capture ability of RLH is larger than that of ILH, the inversion intensity tends to be small. This is due to some of ILH are identified near SBLH. Moreover, the RLH is usually higher than SBLH (Liu et al., 2020; Liu et al., 2021). The aerosols remaining in the RL cause that AOD below RLH is larger than that of ILH. By contrast, the aerosol capture ability of MLH is smaller than that of ILH when the temperature inversion intensity is small. This is due to the MLH is generally lower than ILH. Although aerosols can break through the IL and form higher ML in some cases, in general the AOD below MLH is larger than that of ILH.

5. Conclusions

In this study, the relationship between atmospheric boundary layer and temperature inversion layer was investigated based on the MPL and RS measurements from May 2015 to July 2016 at ARM SGP site. The frequency of occurrence and the aerosol capture capabilities of different layers are analyzed in detail.

The main conclusions are summarized as follows: first, the boundary layer structure can be obtained from aerosol backscatter profiles even without the IL structure. In contrast, the appearance of the IL means that there is a high probability (more than 80%) that the top of the aerosol layer will appear near the ILH. Moreover, the probability of aerosol layer top appearing near the ILH gradually increases with the temperature inversion intensity increased. It indicates that the strong IL can effectively capture aerosols, change the vertical distribution of aerosols, and then affect the inversion of the boundary layer height from lidar data. Then, the relative error between different boundary layer height and ILH

under different ΔT conditions. The result indicates that the ILH is generally higher than the height of boundary layers, and this phenomenon becomes more obvious with the ΔT increased. Finally, we find that the temperature inversion intensity is a key factor in determining the aerosol capture ability. When the temperature inversion intensity is large ($\Delta T > 2^\circ\text{C}$ or $\Delta Z > 0.2 \text{ km}$), the aerosol capture ability of RLH or MLH is similar to that of ILH. By contrast, when the temperature inversion intensity is small, the aerosol capture ability of RLH (MLH) is larger (smaller) than that of ILH. It indicates that the aerosols are mainly concentrated below ILH during the daytime and below RLH at nighttime. These findings have implications for improving our understanding of the vertical distribution of aerosols and its controlling factors.

Author statement

The study was completed with cooperation between all authors. Yingying Ma and Boming Liu designed the research topic; Xin Ma and Boming Liu conducted the experiment and wrote the paper; Hui Li, Shikuan Jin, Ruonan Fan and Wei Gong checked the experimental results.

Declaration of Competing Interest

The authors declare that they have no known competing financial interests or personal relationships that could have appeared to influence the work reported in this paper.

Acknowledgments

This work was financially supported by the National Natural Science Foundation of China under Grant 42001291 and in part by the Project through the China Postdoctoral Science Foundation under Grant 2020M682485.

Appendix A. Supplementary data

Supplementary data to this article can be found online at <https://doi.org/10.1016/j.atmosres.2022.106121>.

References

- Bourgeois, Q., Ekman, A.M., Renard, J.B., Krejci, R., Devasthale, A., Bender, F.A.M., Tackett, J.L., 2018. How much of the global aerosol optical depth is found in the boundary layer and free troposphere? *Atmos. Chem. Phys.* 18 (10), 7709–7720.
- Campbell, J.R., Hlavka, D.L., Welton, E.J., Flynn, C.J., Turner, D.D., Spinharne, J.D., Scott, V.S., Hwang, I.H., 2002. Full-time, eye-safe cloud and aerosol lidar observation at atmospheric radiation measurement program sites: instruments and data processing. *J. Atmos. Ocean. Technol.* 19, 431–442.
- Campbell, J.R., Welton, E.J., Spinharne, J.D., Ji, Q., Tsay, S.C., Piketh, S.J., Barenbrug, M., Holben, B.N., 2003. Micropulse lidar observations of tropospheric aerosols over northeastern South Africa during the ARREX and SAFARI 2000 dry season experiments. *J. Geophys. Res.-Atmos.* 108.
- Che, H., Xia, X., Zhu, J., et al., 2014. Column aerosol optical properties and aerosol radiative forcing during a serious haze-fog month over North China Plain in 2013 based on ground-based sunphotometer measurements. *Atmos. Chem. Phys.* 14 (4), 2125–2138.
- Ding, A.J., Huang, X., Nie, W., Sun, J.N., Kerminen, V.M., Petäjä, T., Chi, X.G., 2016. Enhanced haze pollution by black carbon in megacities in China. *Geophys. Res. Lett.* 43 (6), 2873–2879.
- Fan, W., Qin, K., Xu, J., Yuan, L., Li, D., Jin, Z., Zhang, K., 2019. Aerosol vertical distribution and sources estimation at a site of the Yangtze River Delta region of China. *Atmos. Res.* 217, 128–136.
- Fernald, F.G., 1984. Analysis of atmospheric lidar observations: some comments. *Appl. Opt.* 23, 652.
- Guo, J., Liu, H., Wang, F., Huang, J., Xia, F., Lou, M., Yung, Y.L., 2016. Three-dimensional structure of aerosol in China: a perspective from multi-satellite observations. *Atmos. Res.* 178, 580–589.
- Guo, J., Su, T., Chen, D., Wang, J., Li, Z., Lv, Y., Zhai, P., 2019. Declining summertime local-scale precipitation frequency over China and the United States, 1981–2012: the disparate roles of aerosols. *Geophys. Res. Lett.* 46 (22), 13281–13289.
- Guo, J., Chen, X., Su, T., Liu, L., Zheng, Y., Chen, D., et al., 2020. The climatology of lower tropospheric temperature inversions in China from radiosonde measurements: Roles of black carbon, local meteorology, and large-scale subsidence. *J. Clim.* 33 (21), 9327–9350. <https://doi.org/10.1175/JCLI-D-19-0278.1>.
- Guo, J., Liu, B., Gong, W., Shi, L., Zhang, Y., Ma, Y., Xu, X., 2021. First comparison of wind observations from ESA's satellite mission Aeolus and ground-based radar wind profiler network of China. *Atmos. Chem. Phys.* 21 (4), 2945–2958.
- Kafle, D.N., Coulter, R.L., 2013. Micropulse lidar-derived aerosol optical depth climatology at ARM sites worldwide. *J. Geophys. Res.-Atmos.* 118 (13), 7293–7308.
- Kahl, J.D., 1990. Characteristics of the low-level temperature inversion along the Alaskan Arctic Coast. *Int. J. Climatol.* 10 (5), 537–548. <https://doi.org/10.1002/joc.3370100509>.
- Koren, I., Dagan, G., Altaratz, O., 2014. From aerosol-limited to invigoration of warm convective clouds. *science* 344 (6188), 1143–1146.
- Li, H., Liu, B., Ma, X., Jin, S., Ma, Y., Zhao, Y., Gong, W., 2021. Evaluation of retrieval methods for planetary boundary layer height based on radiosonde data. *Atmos. Meas. Tech.* 14, 5977–5986. <https://doi.org/10.5194/amt-14-5977-2021>.
- Liu, B., Ma, Y., Gong, W., Zhang, M., 2017. Observations of aerosol color ratio and depolarization ratio over Wuhan. *Atmos. Pollut. Res.* 8 (6), 1113–1122.
- Liu, B., Ma, Y., Gong, W., Zhang, M., Yang, J., 2018. Study of continuous air pollution in winter over Wuhan based on ground-based and satellite observations. *Atmos. Pollut. Res.* 9 (1), 156–165.
- Liu, B., Ma, Y., Gong, W., Zhang, M., Shi, Y., 2019. The relationship between black carbon and atmospheric boundary layer height. *Atmos. Pollut. Res.* 10 (1), 65–72.
- Liu, B., Ma, Y., Shi, Y., Jin, S., Jin, Y., Gong, W., 2020. The characteristics and sources of the aerosols within the nocturnal residual layer over Wuhan, China. *Atmos. Res.* 241, 104959.
- Liu, Y., Tang, G., Wang, M., Liu, B., Hu, B., Chen, Q., Wang, Y., 2021. Impact of residual layer transport on air pollution in Beijing, China. *Environ. Pollut.* 271, 116325.
- Ma, Y., Ye, J., Xin, J., Zhang, W., Vilà-Guerau de Arellano, J., Wang, S., Martin, S.T., 2020. The stove, dome, and umbrella effects of atmospheric aerosol on the development of the planetary boundary layer in hazy regions. *Geophys. Res. Lett.* 47 (13), e2020GL087373.
- Ma, X., Jiang, W., Li, H., Ma, Y., Jin, S., Liu, B., Gong, W., 2021a. Variations in nocturnal residual layer height and its effects on surface PM2.5 over Wuhan, China. *Remote Sens.* 13 (22), 4717.
- Ma, Y., Zhu, Y., Liu, B., Li, H., Jin, S., Zhang, Y., Gong, W., 2021b. Estimation of the vertical distribution of particle matter (PM2.5) concentration and its transport flux from lidar measurements based on machine learning algorithms. *Atmos. Chem. Phys.* 21 (22), 17003–17016.
- Ma, Y., Xin, J., Wang, Z., Tian, Y., Wu, L., Tang, G., Martin, S.T., 2022. How do aerosols above the residual layer affect the planetary boundary layer height? *Sci. Total Environ.* 814, 151953.
- Prasad, P., Basha, G., Ratnam, M.V., 2022. Is the atmospheric boundary layer altitude or the strong thermal inversions that control the vertical extent of aerosols? *Sci. Total Environ.* 802, 149758.
- Ramanathan, V., Crutzen, P.J., Kiehl, J.T., et al., 2001. Aerosols, climate, and the hydrological cycle. *Science* 294 (5549), 2119–2124.
- Seibert, P., Beyrich, F., Gryning, S.E., Joffre, S., Rasmussen, A., Tercier, P., 2000. Review and intercomparison of operational methods for the determination of the mixing height. *Atmos. Environ.* 34, 1001–1027.
- Serreze, M.C., Schnell, R.C., Kahl, J.D., 1992. Low-level temperature inversions of the Eurasian Arctic and comparisons with soviet drifting station data. *J. Clim.* 5, 615–629. [https://doi.org/10.1175/1520-0442\(1992\)005,0615:LTIOT.2.0.CO;2](https://doi.org/10.1175/1520-0442(1992)005,0615:LTIOT.2.0.CO;2).
- Shi, Y., Liu, B., Chen, S., Gong, W., Ma, Y., Zhang, M., Jin, Y., 2020. Characteristics of aerosol within the nocturnal residual layer and its effects on surface PM2.5 over China. *Atmos. Environ.* 241, 117841.
- Shi, T., Han, G., Ma, X., Gong, W., Chen, W., Liu, J., Bu, L., 2021. Quantifying CO₂ uptakes over oceans using LIDAR: a tentative experiment in Bohai bay. *Geophys. Res. Lett.* 48 (9), 2020GL091160.
- Steyn, D.G., Baldi, M., Hoff, R.M., 1999. The detection of mixed layer depth and entrainment zone thickness from lidar backscatter profiles. *J. Atmos. Ocean. Technol.* 16, 953–959.
- Stull, R.B., 1988. An Introduction to Boundary Layer Meteorology. Kluwer Academic Publishers, Dordrecht and Boston.
- Su, T., Li, Z., Kahn, R., 2020. A new method to retrieve the diurnal variability of planetary boundary layer height from lidar under different thermodynamic stability conditions. *Remote Sens. Environ.* 237, 111519.
- Sun, Y.W., Sun, X., Yin, Y., Han, Y., Dong, X.B., Jiang, Y., Zhao, Z.J., 2012. Aerosol distribution in North China Plain under different weather conditions. *China Environ. Sci.* 32, 1736–1743.
- Sun, Y., Song, T., Tang, G., Wang, Y., 2013. The vertical distribution of PM2.5 and boundary-layer structure during summer haze in Beijing. *Atmos. Environ.* 74, 413–421.
- Tang, G., Zhang, J., Zhu, X., Song, T., Mükel, C., Hu, B., Wang, Y., 2016. Mixing layer height and its implications for air pollution over Beijing, China. *Atmos. Chem. Phys.* 16 (4), 2459–2475.
- Wallace, J.P., Kanaroglou, P., 2009. The effect of temperature inversions on ground-level nitrogen dioxide (NO₂) and fine particulate matter (PM2.5) using temperature profiles from the Atmospheric infrared Sounder (AIRS). *Sci. Total Environ.* 407, 18, 5085–5095. <https://doi.org/10.1016/j.scitotenv.2009.05.050>.
- Wang, H., Sun, Z., Li, H., Gao, Y., Wu, J., Cheng, T., 2018. Vertical-distribution characteristics of atmospheric aerosols under different thermodynamic conditions in Beijing. *Aerosol Air Qual. Res.* 18, 2775–2787. <https://doi.org/10.4209/aaqr.2018.03.0078>.
- Wang, W., He, J., Miao, Z., Du, L., 2021. Space-Time Linear Mixed-Effects (STLME) model for mapping hourly fine particulate loadings in the Beijing-Tianjin-Hebei region, China. *J. Clean. Prod.* 292, 125993.

- Welton, E.J., Campbell, J.R., 2002. Micropulse lidar signals: uncertainty analysis. *J. Atmos. Ocean. Technol.* 19, 2089–2094.
- Welton, E.J., Voss, K.J., Gordon, H.R., Maring, H., Smirnov, A., Holben, B., et al., 2000. Ground-based lidar measurements of aerosols during ACE-2: instrument description, results, and comparisons with other ground-based and airborne measurements. *Tellus B* 52 (2), 636–651.
- Welton, E.J., Campbell, J.R., Spinhirne, J.D., Scott, V.S., 2001. In: Singh, U.N., Itabe, T., Sugimoto, N. (Eds.), Globalmonitoring of Clouds and Aerosols Using a Network of Micro-Pulse Lidarsystems, inLidar Remote Sensing for Industry and Environmental Mon-Itoring, vol. 4153. Proc. SPIE, Sendai, Japan, pp. 151–158.
- Whiteman, D.N., Demoz, B., Di Girolamo, P., Comer, J., Veselovskii, I., Evans, K., Wang, Z., Cadirola, M., Rush, K., Schwemmer, G., Gentry, B., Melfi, S.H., Mielke, B., Venable, D., Van Hove, T., 2006. Raman lidar measurements during the International H2O Project. Part I: instrumentation and analysis techniques. *J. Atmos. Ocean. Technol.* 23, 157–169.
- Yang, J., Yang, S., Zhang, Y., Shi, S., Du, L., 2021. Improving characteristic band selection in leaf biochemical property estimation considering interrelations among biochemical parameters based on the PROSPECT-D model. *Opt. Express* 29 (1), 400–414.
- Yin, P., Guo, J., Wang, L., Fan, W., Lu, F., Guo, M., Dong, Z., 2020. Higher risk of cardiovascular disease associated with smaller size-fractioned particulate matter. *Environ. Sci. Technol. Lett.* 7 (2), 95–101.
- Zhang, Q., Quan, J., Tie, X., Huang, M., Ma, X., 2011. Impact of aerosol particles on cloud formation: Aircraft measurements in China. *Atmos. Environ.* 45, 665–672. <https://doi.org/10.1016/j.atmosenv.2010.10.025>.
- Zhao, D., Xin, J., Gong, C., Quan, J., Wang, Y., Tang, G., Ma, Y., 2021. The impact threshold of the aerosol radiative forcing on the boundary layer structure in the pollution region. *Atmos. Chem. Phys.* 21 (7), 5739–5753.
- Zhu, Y., Ma, Y., Liu, B., Xu, X., Jin, S., Gong, W., 2021. Retrieving the vertical distribution of PM_{2.5} mass concentration from lidar via a random forest model. In: *IEEE Transactions on Geoscience and Remote Sensing*.